water

MDPI

Article

Prediction of the Cavitation over a Twisted Hydrofoil Considering the Nuclei Fraction Sensitivity at 4000 m Altitude Level

Hongying Luo [1] and Ran Tao [2,3,*]

[1] School of Water Resources and Civil Engineering, Tibet Agriculture & Animal Husbandry University, Linzhi 860000, China; xznmxylhy@163.com
[2] College of Water Resources and Civil Engineering, China Agricultural University, Beijing 100083, China
[3] Beijing Engineering Research Center of Safety and Energy Saving Technology for Water Supply Network System, China Agricultural University, Beijing 100083, China
* Correspondence: randytao@cau.edu.cn

Abstract: Cavitation phenomenon is important in hydraulic turbomachineries. With the construction of pumping stations and hydro power stations on plateau, the influence of nuclei fraction on cavitation becomes important. As a simplified model, a twisted hydrofoil was used in this study to understand the cavitation behaviors on pump impeller blade and turbine runner blade at different altitude levels. The altitudes of 0 m, 1000 m, 2000 m, 3000 m and 4000 m were comparatively studied for simulating the plateau situation. Results show that the cavitation volume proportion f_{cav} increases with the decreasing of cavitation coefficient C_σ. At a specific C_σ, high altitude and few nuclei will cause smaller size of cavitation. The smaller C_σ is, the higher the sensitivity Δf_{cav} is. The larger C_σ is, the higher the relative sensitivity $\Delta f_{cav}{}^*$ is. On the twisted foil, flow incidence angle increases from the sidewall to mid-span with the decreasing of the local minimum pressure. When C_σ is continually decreasing, the size of cavitation extends in spanwise, streamwise and thickness directions. The cavity is broken by the backward-jet flow when C_σ becomes small. A tail generates and the cavity becomes relatively unstable. This study will provide reference for evaluating the cavitation status of the water pumps and hydroturbines installed on a plateau with high altitude level.

Keywords: cavitation; detaches eddy simulation; twisted hydrofoil; pressure distribution; high altitude

Citation: Luo, H.; Tao, R. Prediction of the Cavitation over a Twisted Hydrofoil Considering the Nuclei Fraction Sensitivity at 4000 m Altitude Level. *Water* **2021**, *13*, 1938. https://doi.org/10.3390/w13141938

Academic Editor: Michele La Rocca

Received: 9 June 2021
Accepted: 11 July 2021
Published: 13 July 2021

1. Introduction

Cavitation is a commonly seen phenomenon in hydrodynamic turbomachinery cases such as pumps and hydroturbines [1–3]. It usually has bad influences including noise [4], vibration [5] and material damage [6]. For this reason, cavitating flow in hydraulic turbomachinery has been widely studied by researchers to understand its mechanism, behavior and influence. As a simplification of the blade of hydraulic turbomachinery, hydrofoil is usually used in the study of cavitation and cavitating flow. Arabnejad et al. [7] and Tao et al. [8] investigated the leading-edge cavitation over symmetric hydrofoils. Different types of leading-edge cavitation are discussed in detail. Dreyer et al. [9] and Guo et al. [10] used hydrofoil to have a better study of the tip-leakage cavitation of blade. Cavitation happening in the tip-leakage vortex was studied to help the anti-cavitation design of axial-flow hydraulic runners. Escaler et al. [11] and Melissaris et al. [12] used hydrofoil models to study the cavitation erosion behavior of hydraulic runner blades. The erosion risk can be well evaluated.

In these previous studies, cavitation on hydrofoil surfaces is mainly found related to the local flow separation and pressure drop [13]. Under different flow conditions, cavitation performs in different types. If the size of cavitation is small and flow is stable, the cavitation bubble will also stably attach on the surface [14]. If local flow is unstable and the size of cavitation becomes large, the cavitation bubble will move with flow as a

cloudy cavitation [15]. Generally, the status of cavitation on impeller blade or hydrofoil is strongly related to the blade (foil) profile, local flow stability and the size of cavitation itself. As another important factor, the nuclei fraction will also affect the status of cavitation [16]. However, this factor is usually ignored, because the nuclei fraction in water medium has only a slight influence on cavitation.

Currently, more and more pumping stations and water power stations are constructed on plateau [17–19]. There are many stations built above 3000 m or even above 4000 m. Thus, the nuclei fraction in water medium is completely different from the situation in low-altitude area. It may have a strong influence on cavitating flow. As a robust and effective way in studying cavitation, the computational fluid dynamics (CFD) tool is widely applied especially for water pumps and hydroturbines [20–24]. Based on CFD, different cavitation models can be supplied to predict the cavitating two-phase flow. Currently, most of the popular cavitation models are based on the Rayleigh–Plesset equation [25], which describes the bubble dynamics under the influence of pressure field. Kubota et al. [26] built–a cavitation model based on the Rayleigh–Plesset equation to calculate the cavitation bubble size and vapor fraction. Considering the influence of compressibility and pressure pulsation caused by turbulence kinetic energy, Singhal et al. [27] supposed the full cavitation model as an improvement in the simulation of cavitating flow. Schnerr and Sauer [28] focused on the modeling of the mass transfer rate between gas phase and liquid phase. The Schnerr–Sauer model is built to treat the cavitating flow as a mixture of liquid and a large number of gas bubbles. Zwart, Gerber and Belamri [29] improved the cavitation prediction method based on the Kubota model. In the Zwart model, the volume fraction terms are corrected because gas volume will vary with the medium density. Kunz et al. [30] considered the difference between the form and collapse of cavitation bubble. They introduced the Kunz model, which describes the liquid–gas phase change and gas-liquid phase change in different ways. In general, all these models consider the influence of nuclei fraction on cavitation. Hence, it will be feasible to discuss the influence of nuclei fraction in simulating the cavitation at different altitude levels.

However, there is no article that analyzes the influence of nuclei fraction in simulating the cavitation in hydraulic turbomachineries. Cavitation in hydraulic turbomachinery is strongly relative to the internal complex flow regimes like vortex, back flow, jet-wake, stall-cells and other pressure drop cases [31]. In this case, a twisted hydrofoil [32] was used as a simplified case to have a sensitivity analysis of nuclei fraction in simulating the cavitation at different altitude levels. Considering the altitude of the Qinghai–Tibet Plateau, which is over 4000 m, the air pressure is strongly different from that in the low-altitude area [33]. According to Henry's law, the nuclei fraction strongly varies from low-altitude area to a 4000 m plateau. This study will comparatively analyze the cavitation at high altitude level. With the nuclei fraction at 4000 m, the turbulent flow and development of cavitation over the twisted hydrofoil was analyzed in detail. It will provide a good reference for water pumps and hydroturbines for high-altitude levels considering the anti-cavitation issue.

2. Numerical Methods

2.1. Numerical Method for Turbulent Flow

Considering the strong adverse pressure gradient in the main flow region and the shear flow near the, the Shear Stress Transport (SST) model-based Detached Eddy Simulation (DES) method [34,35] is used as the numerical method for turbulent flow in CFD simulation. The k and ω equations of SST model can be written as follows:

$$\frac{\partial(\rho k)}{\partial t} + \frac{\partial(\rho u_i k)}{\partial x_i} = P - \frac{\rho k^{3/2}}{l_{k-\omega}} + \frac{\partial}{\partial x_i}\left[(\mu + \sigma_k \mu_t)\frac{\partial k}{\partial x_i}\right] \quad (1)$$

$$\frac{\partial(\rho \omega)}{\partial t} + \frac{\partial(\rho u_i \omega)}{\partial x_i} = C_\omega P - \beta \rho \omega^2 + \frac{\partial}{\partial x_i}\left[(\mu_l + \sigma_\omega \mu_t)\frac{\partial \omega}{\partial x_i}\right] + 2(1 - F_1)\frac{\rho \sigma_{\omega 2}}{\omega}\frac{\partial k}{\partial x_i}\frac{\partial \omega}{\partial x_i} \quad (2)$$

where ρ is density, P is the turbulence production term, μ is dynamic viscosity, μ_t is eddy viscosity, σ is model constant, C_ω is the turbulence dissipation term, F_1 is the zonal blending function, $l_{k-\omega}$ is called the turbulence scale that $l_{k-\omega} = k^{1/2}\beta_k\omega$, where β_k is the model constant. The DES method uses a zonal treatment term that $\min(l_{k-\omega}, C_{DES}{\cdot}L_{mesh})$, where L_{mesh} is the maximum mesh element dimension and C_{DES} is a constant. When $l_{k-\omega}$ is larger than $C_{DES}{\cdot}L_{mesh}$, Large Eddy Simulation will be activated. Otherwise, SST model is used in the Reynolds-averaged mode.

2.2. Cavitation Model

The Zwart model [29] is a widely used cavitation model in current CFD simulations of cavitating two-phase flow. It is based on the Rayleigh–Plesset bubble dynamic equation to describe the mass transfer. It has the advantage that the sensitivity of cavitation vapor volume due to density change is considered. The requirement of computational cost when reasonable is used for engineering simulations. Therefore, it is applied as the cavitation model in this case. The rate of mass transfer $\dot{m}$ can be expressed as:

$$\dot{m} = \begin{cases} -F_e \frac{3 f_{vnuc}(1-\alpha)\rho_v}{R_B}\sqrt{\frac{2}{3}\frac{p_v - p}{\rho_i}} & \text{if } p < p_v \\ F_c \frac{3\alpha\rho_v}{R_B}\sqrt{\frac{2}{3}\frac{p - p_v}{\rho_i}} & \text{if } p > p_v \end{cases} \tag{3}$$

where p_v is the saturation pressure, ρ_v is the vapor density, f_{vnuc} is the nuclei volume fraction, R_B is the nuclei average radius, F_e and F_c are coefficients of evaporization and condensation which are commonly $F_e = 50$ and $F_c = 0.01$.

2.3. Vapor Volume Fraction

According to Henry's law, the gas dissolved as nuclei in liquid is proportional to the gas pressure over the liquid surface. Based on the data statistics on the Qinghai–Tibet Plateau [33], the atmosphere pressure P_{atm} and altitude H_{alt} have the approximate relationship as:

$$P_{atm} = C_{d1} + C_{d2}H_{alt} + C_{d3}H_{alt}^2 \tag{4}$$

where C_d are constants that $C_{d1} = 1.013 \times 10^5$, $C_{d2} = 1.259 \times 10^1$, $C_{d3} = 6.476 \times 10^{-4}$. Based on Henry's law, the nuclei volume fraction f_{vnuc} will be different if the altitude H_{alt} is different. The original f_{vnuc} at $H_{alt} = 0$ m is 5×10^{-4}. In this case, the altitude conditions that $H_{alt} = 0$ m, 1000 m, 2000 m, 3000 m and 4000 m are comparatively studied. Therefore, the values of f_{vnuc} are listed in Table 1.

Table 1. Nuclei volume fraction value in comparative CFD simulations.

Altitude H_{alt}	Nuclei Volume Fraction f_{vnuc}
0 m	5×10^{-4}
1000 m	4.38×10^{-4}
2000 m	3.88×10^{-4}
3000 m	3.48×10^{-4}
4000 m	3.01×10^{-4}

3. Case and Setup

3.1. Important Dimensionless Parameters

In this study, the hydrofoil case was discussed. To investigate the cavitating flow, two dimensionless parameters are defined as follows. Firstly, the fundamental parameter in the cavitation description is the cavitation coefficient C_σ:

$$C_\sigma = \frac{2\left(p_{ref} - p_v\right)}{\rho v_{ref}^2} \tag{5}$$

where p_v is the saturation pressure, p_{ref} and v_{ref} are reference pressure and velocity, respectively, which are usually measured at the upstream of hydrofoil, ρ is density. Therefore, C_σ can be adjusted by changing the value of p_{ref}. Secondly, the pressure coefficient C_p can be defined as:

$$C_p = \frac{2\left(p_v - p_{ref}\right)}{\rho v_{ref}^2} \tag{6}$$

where p is pressure. Therefore, the same C_σ values can be compared for different altitudes with considering that the altitude caused a difference on nuclei volume fraction f_{vnuc}.

3.2. Flow Domain of Hydrofoil

In this study, the Delft Twist 11 hydrofoil [32,36] was used based on the NACA0009 profile. This symmetric NACA 4-digit foil profile can be expressed as follows:

$$\pm\frac{Y}{c} = \frac{Y_m}{C_a \cdot c}\left[C_{b1}\sqrt{\frac{X}{c}} - C_{b2}\left(\frac{X}{c}\right) - C_{b3}\left(\frac{X}{c}\right)^2 + C_{b4}\left(\frac{X}{c}\right)^3 - C_{b5}\left(\frac{X}{c}\right)^4\right] \tag{7}$$

where c is the total camber length, X is the position along camber direction, Y is the thickness, Y_m is the maximum thickness of foil. Parameter C_a and C_b are constants that C_a = 0.2, C_{b1} = 0.2969, C_{b2} = 0.126, C_{b3} = 0.3516, C_{b4} = 0.2843 and C_{b5} = 0.1015. This twisted hydrofoil has a different installation angle α at a different span. It has the law of α as:

$$\alpha(s) = \alpha_m\left(2|s-1|^3 - 3(s-1)^2 + 1\right) + a_w \tag{8}$$

where s is the non-dimensionalized spanwise position against the chord length c and here $0 \le s \le 2$. α_m is the maximum installation angle at mid-span, which is 11 degrees. α_w is the installation angle on the wall side, which is −2 degrees in this case.

The 3D flow domain around the twisted hydrofoil is shown in Figure 1, which location in the Cartesian x-y-z coordinate is used for CFD simulation. As shown in Figure 2, c denotes the total chord length of the hydrofoil and c = 1.5 L_{ref}, where L_{ref} is 100 mm. The domain size is L_1 = 10.5 L_{ref}, L_2 = 3.0 L_{ref} and L_3 = 1.5 L_{ref}. The foil center locates 3.0 L_{ref} downstream to the inlet. In this case, the domain is simplified as a half of the entire flow region that $s = z/c$ is within 0~1.

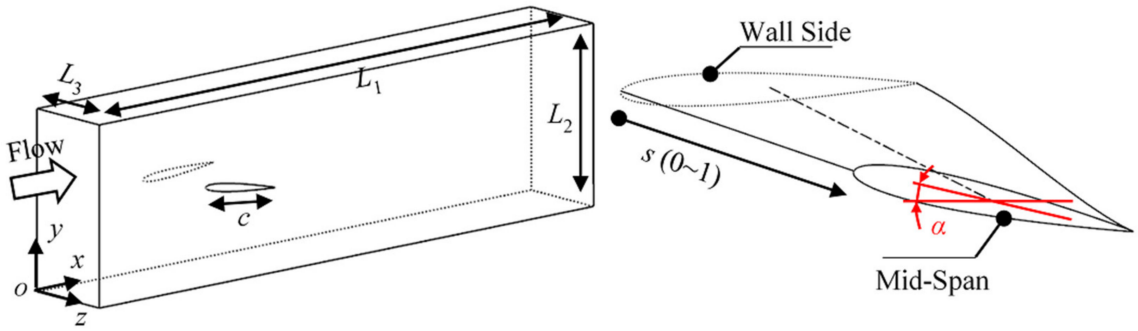

Figure 1. Geometry and size of the flow domain and hydrofoil.

3.3. CFD Setup

The CFD was conducted following the sequence of meshing, setting and solving. The mesh was independence-checked, as shown in Figure 2. The criterion is that the residual of lift/drag ratio is less than 0.001. The final mesh is in the structured type with 2,449,280 nodes and 2,380,744 hexahedral elements. Mesh in the near-wall region was controlled for wall-function where y^+ was from 0.47 to 23.75. As introduced above, the DES method and Zwart cavitation model were used in this numerical study. The fluid is water

at 20 °C. As indicated, boundary conditions are set on the domain including a velocity inlet, a pressure outlet, a symmetry boundary at mid-span, a no-slip wall on foil surface, slip wall boundaries on upper wall, lower wall and side wall. The inlet velocity v_{in} is 6.97 m/s, which means that the Reynolds number Re is 1.05×10^6. The reference location for C_p and C_σ is the inlet boundary. To have a better study of cavitation, the same C_σ situations are compared for different altitude levels. For a specific value of v_{in}, the inlet–outlet pressure difference is almost unchanged. Thus, p_{ref} at inlet can be adjusted to an expectable value by setting a specific pressure value at outlet. Steady-state simulation is firstly conducted. It will converge after the RMS residual of momentum and continuity equation is less than 1×10^{-4} or finish after 1000 iterations. Transient simulation is conducted based on steady-state simulation. The total time is 1s and the time step is 1×10^{-5} s. The maximum iteration number for each time step is 10. The convergence criterion is also RMS residual less than 1×10^{-4}.

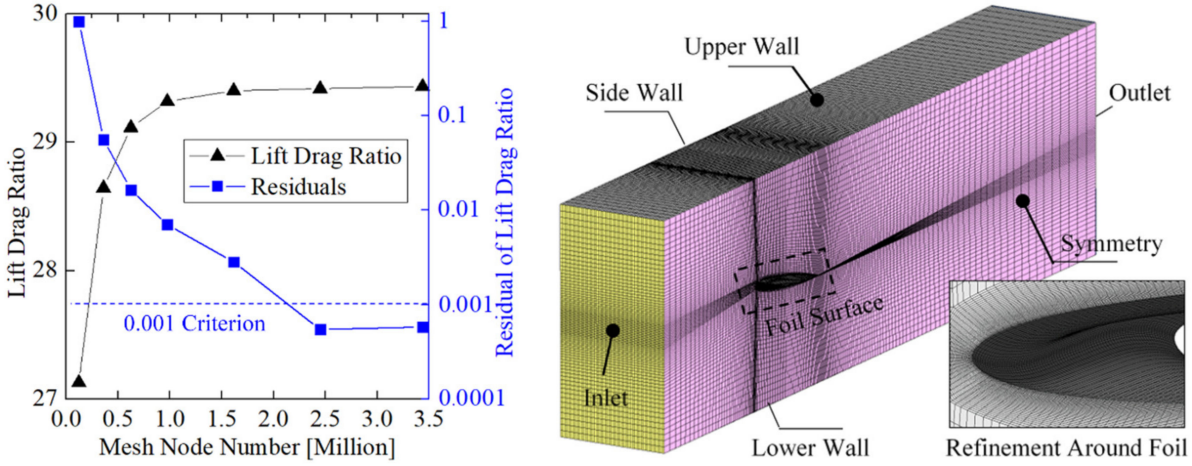

Figure 2. Mesh independence check and the final mesh scheme with the indication of boundaries.

4. Numerical-Experimental Verification

Before analyzing the CFD results, it is necessary to verify the simulation. Figure 3 shows the comparison of pressure coefficient C_p between CFD prediction and experimental data [12,36]. Three different spanwise positions in which s = 0.6, 0.8 and 1.0 are compared, especially focusing on the low-pressure side where cavitation usually occurs. The CFD predicted C_p curves are accurate on the three spanwise surfaces. The CFD simulation can be used for further analyses of the cavitating flow in the following sections.

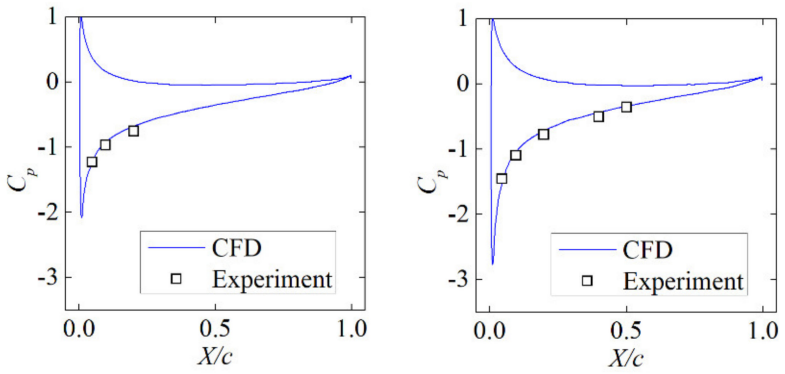

Figure 3. *Cont.*

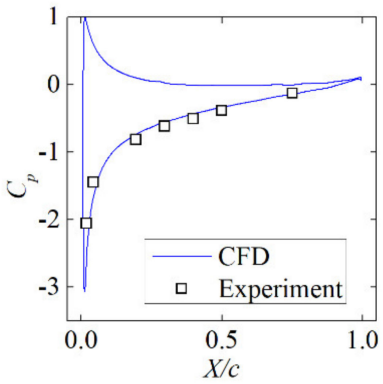

Figure 3. Verification of the CFD prediction on pressure coefficient C_p based on the experimental data [12,34].

5. Cavitation Vapor Proportion at Different Altitudes

5.1. Variation Law

To study the sensitivity of nuclei fraction at different altitudes H_{alt}, the cavitation vapor proportion f_{cav} in the fluid domain is defined as:

$$f_{cav} = V_{cav}/V_{fluid} \tag{9}$$

where V_{cav} is the cavitation vapor volume and V_{fluid} is the fluid domain volume.

Figure 4 shows the comparison of cavitation vapor proportion f_{cav} among different H_{alt} at different C_σ. With the decreasing of C_σ from 2.713 to 1.071, f_{cav} continually increases to a high level. The smaller C_σ is, the quicker f_{cav} increases. It represents the increasing of cavitation vapor in the entire fluid domain. However, there are differences among different H_{alt} situations. Figure 5 shows the cavitation vapor proportion among different H_{alt} at specific C_σ values. The tendency is similar in all the 9 situations that f_{cav} decreases with the increasing of the H_{alt} level.

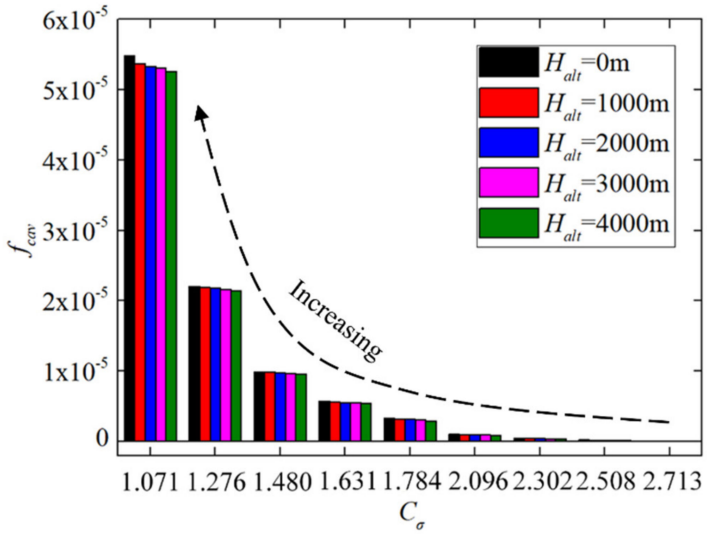

Figure 4. Comparison of cavitation vapor proportion f_{cav} among different H_{alt} at different C_σ.

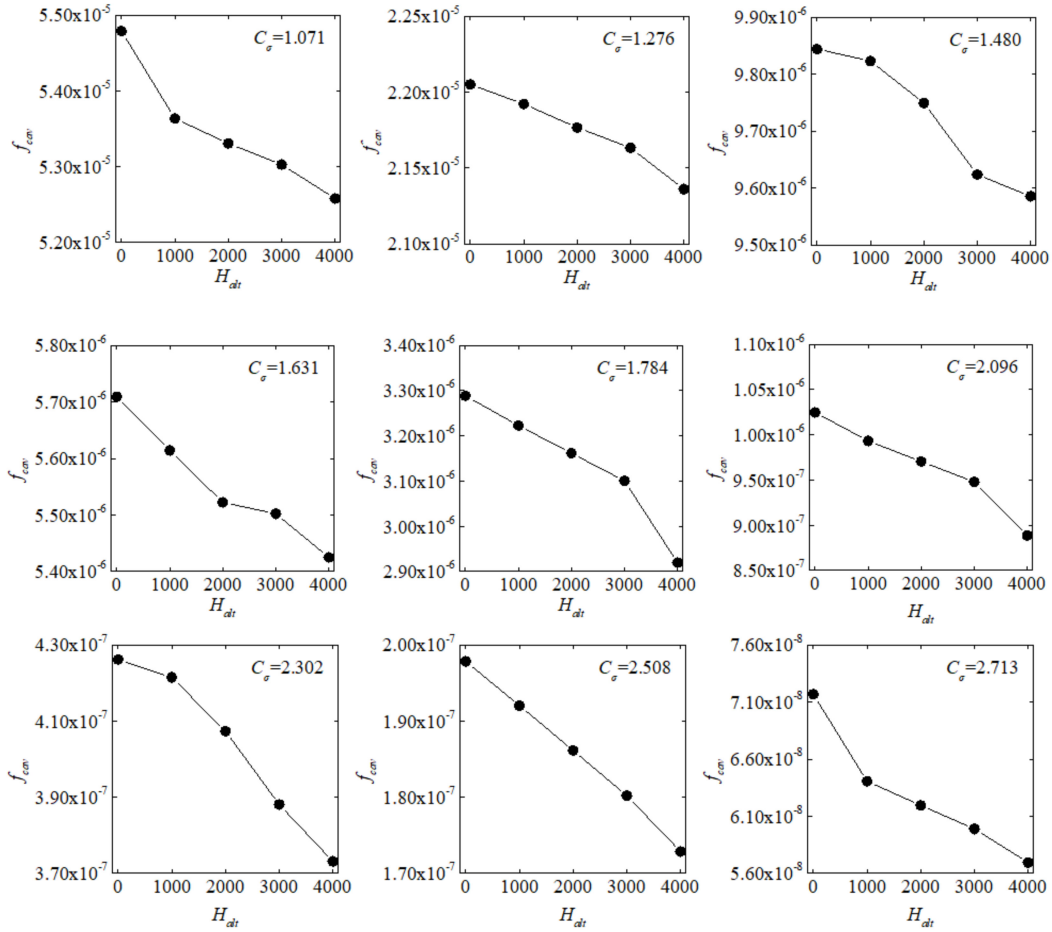

Figure 5. Cavitation vapor proportion among different H_{alt} at a specific C_σ.

5.2. Sensitivity Analysis

Because the size of cavitation is different at different H_{alt}, it is necessary to analyze the sensitivity of f_{cav} on H_{alt} and f_{vnuc}. The difference between maximum and minimum f_{cav} among different H_{alt} at a specific C_σ is defined as the sensitivity Δf_{cav}. For a better comparison, the relative sensitivity $\Delta f_{cav}{}^*$ is defined as:

$$\Delta f_{cav}{}^* = \Delta f_{cav} / f_{cav}{}^a \tag{10}$$

where $f_{cav}{}^a$ is the average vapor proportion of all the 5 H_{alt} situations.

Figure 6 shows the sensitivity analysis of f_{cav} at different C_σ. The H_{alt}-average vapor proportion $f_{cav}{}^a$ shows the same variation tendency as in Figure 4. $f_{cav}{}^a$ increases with the decreasing of C_σ. The sensitivity Δf_{cav} has almost the similar tendency of $f_{cav}{}^a$. The smaller C_σ is, the greater the difference is among different altitudes. However, there is a special local peak region when Δf_{cav} drops to a low level around C_σ = 1.8. It means that the difference between maximum and minimum f_{cav} is locally higher.

When the size of cavitation is small at high C_σ, the absolute difference of f_{cav} among different H_{alt} is also small. Therefore, it is necessary to compare the variation of relative sensitivity $\Delta f_{cav}{}^*$. As shown, the tendency is completely different. It is in a W-shape with two slowly variating regions and two rapidly rising regions, as indicated. The first rapidly rising region is about C_σ = 1.5~1.9. The secondly rapidly rising region is about C_σ = 2.5~2.7. Generally, when the size of cavitation is small, the relative sensitivity $\Delta f_{cav}{}^*$ is higher. In the high altitude plateau area, it is necessary to consider the influence of altitude level on cavitation inception.

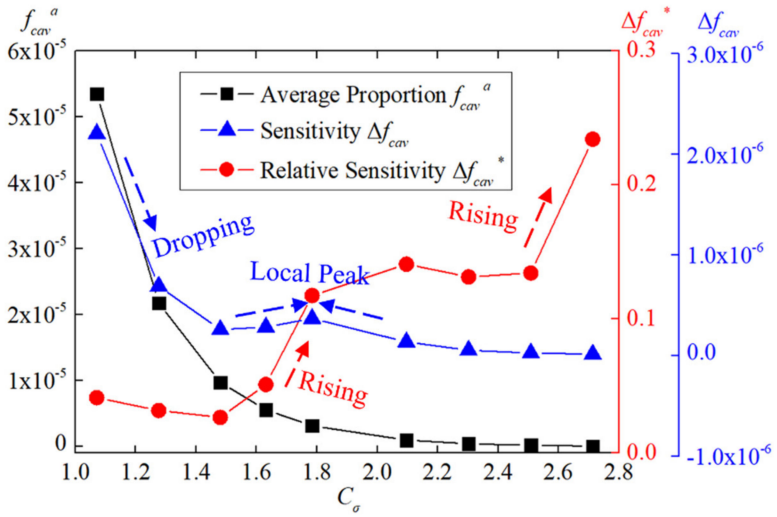

Figure 6. Sensitivity analysis of f_{cav} at different C_σ.

6. Flow Behaviors Considering Altitude Level

6.1. Pressure Distribution Law on Foil Surface

After analyzing the influence of altitude level on the simulation of cavitating flow, it is necessary to study the flow behaviors around the hydrofoil. As is commonly known, cavitation on hydrofoil is strongly related to the pressure distribution. Figure 7 shows the distribution of pressure coefficient C_p on different spanwise positions ($0 \leq s \leq 1$) of foil without considering cavitation. The maximum pressure coefficient C_{pmax} is similar (about 1.0) for different s. This high pressure is because of the local flow striking on the foil lower surface, as shown in Figure 8. The minimum pressure coefficient C_{pmin} varies with s. The larger s is, the smaller C_{pmin} is. This is because of the local flow separation on the foil upper surface, as is also shown in Figure 8.

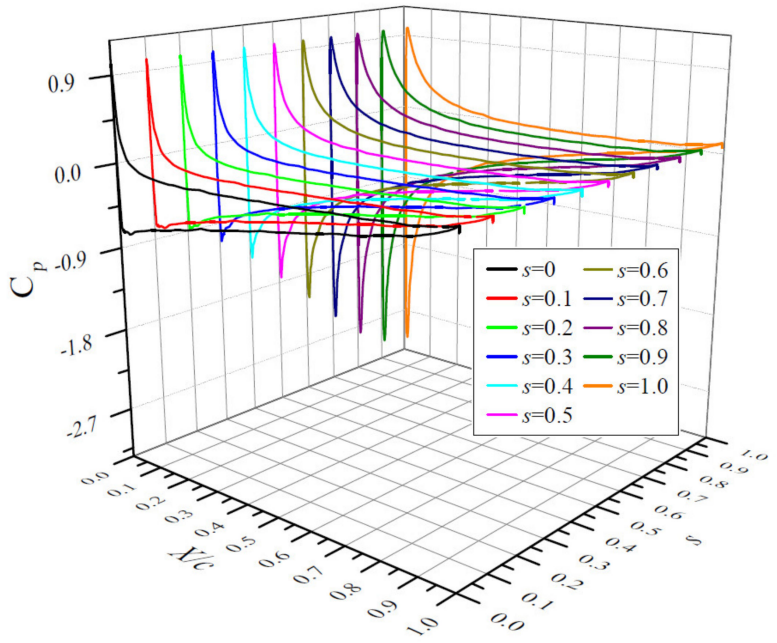

Figure 7. C_p distribution at different spanwise s positions.

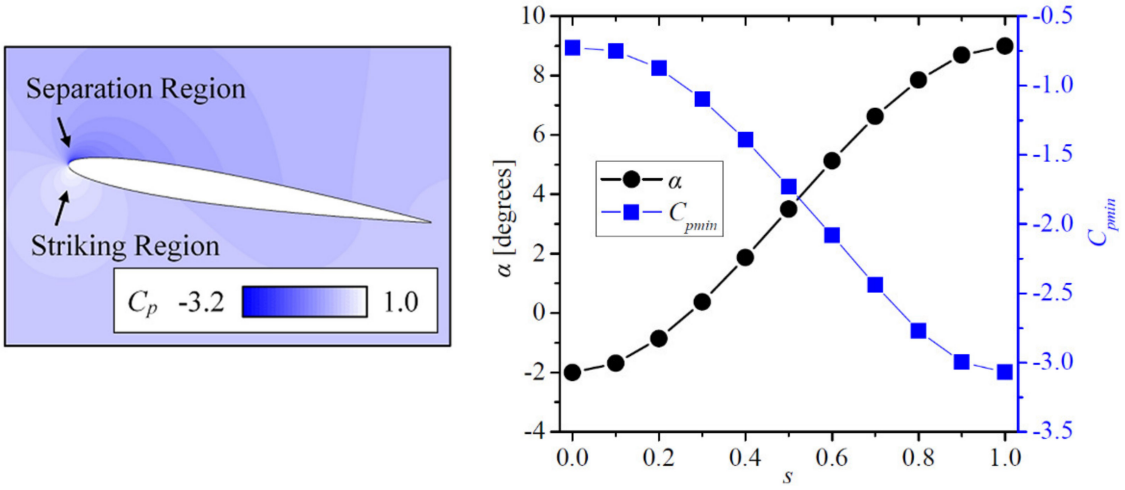

Figure 8. Minimum pressure coefficient C_{pmin} and installation angle α at different spanwise s positions with local contour of C_p on the mid-span plane.

To have a better comparison, Figure 8 shows the minimum pressure coefficient C_{pmin} and installation angle α at different spanwise s positions. There is a significant inverse relationship between C_{pmin} and α. The larger the installation angle is, the larger the flow incidence angle is. It indicates the stronger and stronger flow separation and pressure drop when incidence angle is increasing.

6.2. Turbulent Flow around Foil

To have a better understanding of the pressure drop, Figure 9 shows the velocity coefficient C_v at different spanwise s positions with indication of vectors. The uniformed velocity C_v is defined as:

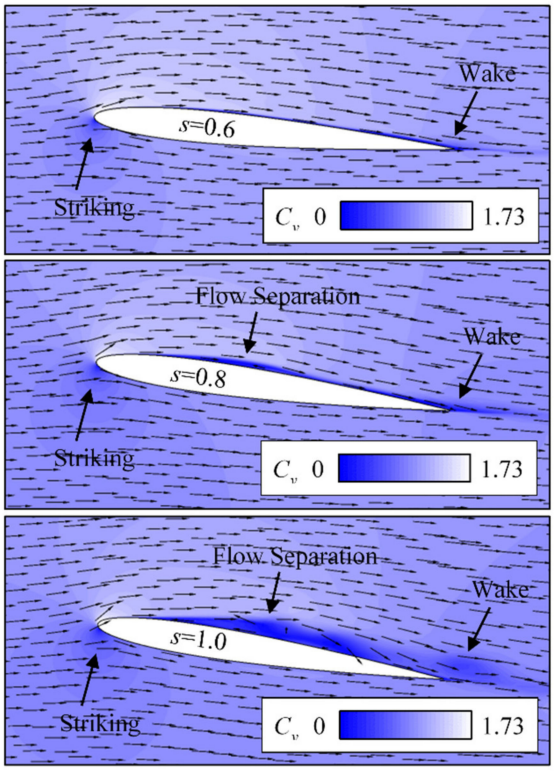

Figure 9. Velocity coefficient C_v at different spanwise s positions with indication of velocity vectors.

$$C_v = v/v_{in} \tag{11}$$

where v is velocity and v_{in} is the velocity at inlet.

At s = 0.6, installation angle α is about 5.13 degrees. Flow attaches well on the foil surface. There are two typical low C_v regions. Firstly, it is the local flow striking region on the leading-edge on the foil lower surface. Secondly, it is the wake region downstream to the foil trailing-edge. At s = 0.8, installation angle α increases to about 7.86 degrees. An obvious flow separation region occurs on the foil upper surface with low C_v. The leading-edge striking region and the trailing-edge wake region are wider. At s = 1.0 (mid-span), installation angle α increases to 9 degrees, which is relatively large. It is obvious that the flow separation region on the foil upper surface is much wider. The leading-edge striking region and the trailing-edge wake region are also wider.

Considering the flow separation and sudden pressure drop at s = 1.0 (mid-span), it is necessary to analyze the local vortex shedding pattern, especially on the foil upper surface. In this case, the velocity helicity H_v is used [37]. It can be non-dimensionalized to the velocity helicity coefficient C_{vhe} by:

$$C_{vhe} = H_v/g \tag{12}$$

where g is the acceleration of gravity.

Figure 10 shows the velocity helicity coefficient C_{vhe} on the mid-span plane and foil upper surface. The vortex-shedding phenomenon can be seen with the indication of the vortex-shedding route (VSR). On the mid-span plane, obvious VSR can be found from leading-edge (LE), along the upper surface, to trailing-edge (TE) and towards downstream. On the foil upper surface, VSR is complex and mainly along the diagonal line from the LE-mid-span corner to the TE-wall corner. Generally speaking, local vortical flow moves along the slope of the twisted foil surface.

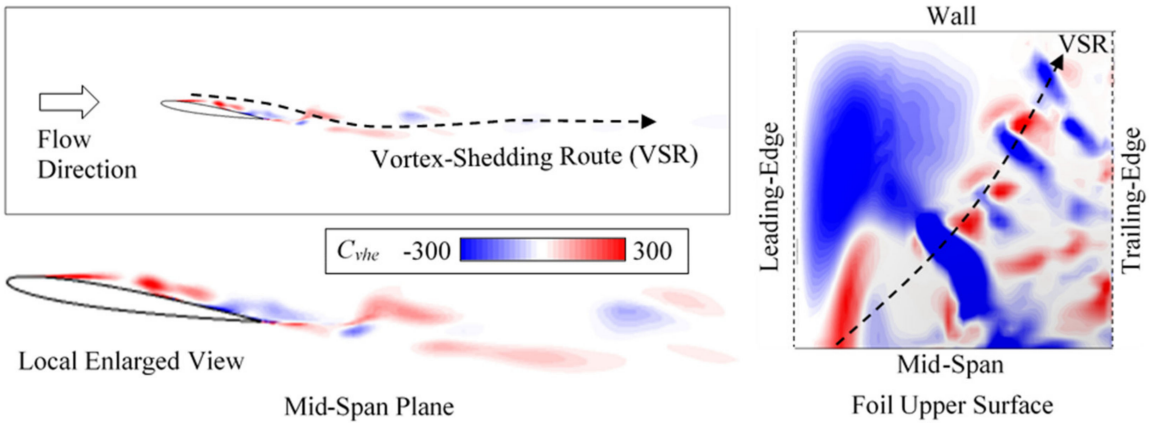

Figure 10. Velocity helicity coefficient C_{vhe} on the mid-span plane and foil upper surface. VSR: vortex-shedding route.

6.3. Development of Cavitation at H_{alt}- = 4000 m

Considering the plateau environment that H_{alt} = 4000 m and $f_{vnuc} = 3.01\times10^{-4}$, the cavitating flow is simulated and analyzed in Figure 11. The development of cavitation is comparatively studied from C_σ = 2.713 to C_σ = 1.071. The scale of cavitation continually increases in different directions. Figure 11 mainly shows the region of cavitation covering on the foil upper surface. Leading-edge (LE) is on the left side. Two parameters are defined to have a quantitative comparison. One is the length of cavity-covered area l_{cav} and another is the width of cavity-covered area w_{cav}. Figure 11 also includes the mid-span view of cavitation. Two parameters are defined in this view. One is the maximum thickness of cavity on mid-span t_{cav}. Another is the total length of the attached part of the cavity on

mid-span, which is denoted as $l_{cav}{}^{*}$. In general, l_{cav}, w_{cav}, t_{cav} and $l_{cav}{}^{*}$ increase with the decreasing of cavitation coefficient C_σ.

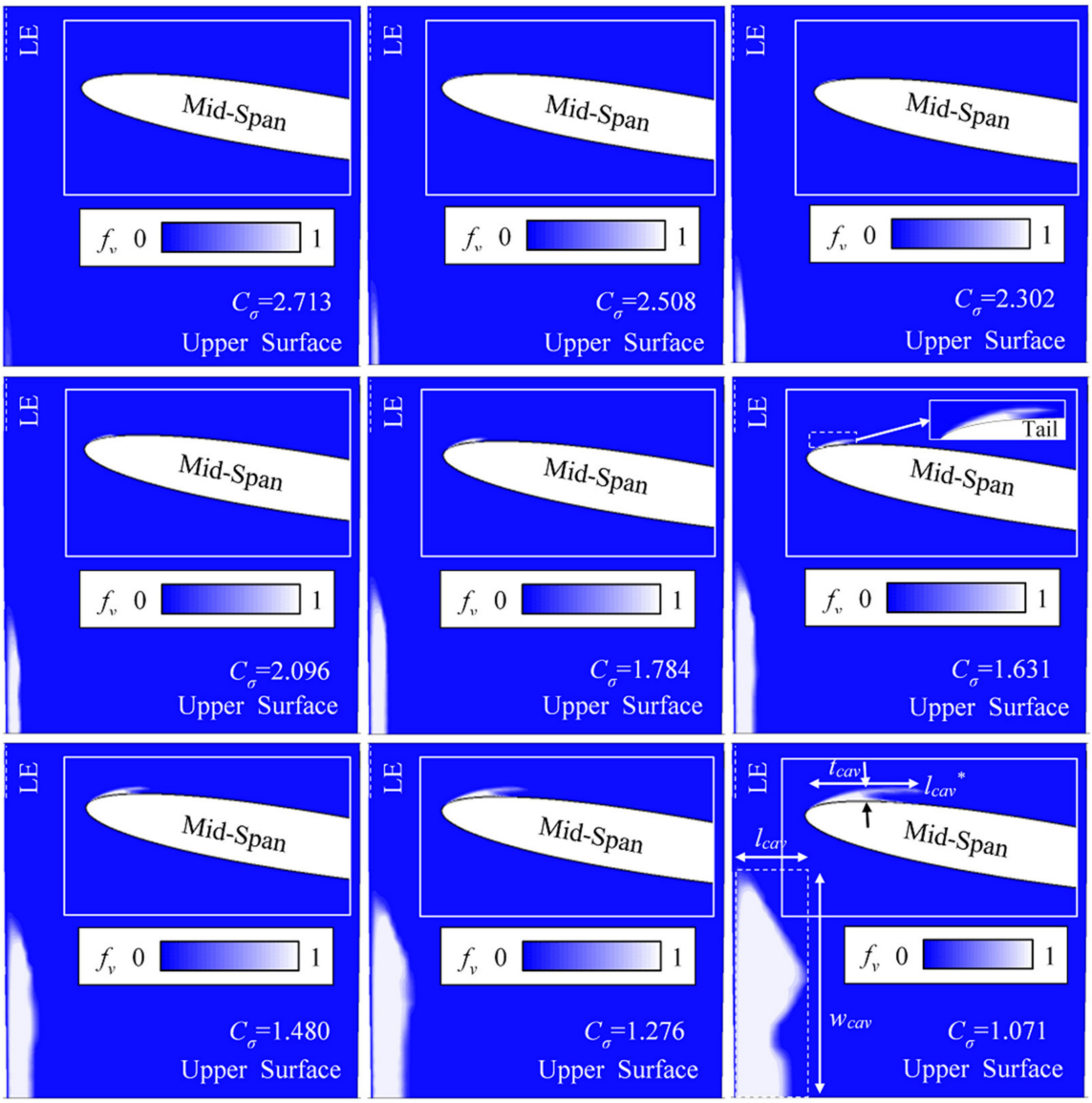

Figure 11. Variation of the cavitation vapor volume fraction f_v on the mid-span plane and foil upper surface with the decreasing of cavitation coefficient C_σ. LE: leading-edge.

To have a better analysis, the variation of l_{cav}, w_{cav}, t_{cav} and $l_{cav}{}^{*}$ are compared in Figure 12. These four parameters are normalized against the foil chord length c. The growth rate $d\varphi/dC_\sigma$ is also analyzed between each two conditions.

For the length of cavity-covered area on foil upper surface l_{cav}, the growth rate is relatively low, within C_σ = 2.173~1.784. The value of $d(l_{cav}/c)/dC_\sigma$ is lower than 0.05. The value of l_{cav}/c increases from about 0.026 to about 0.051. When C_σ is smaller than 1.784, the growth rate of l_{cav} becomes much higher. The value of $d(l_{cav}/c)/dC_\sigma$ is about 0.09~0.40. From C_σ = 1.784 to C_σ = 1.071, the value of l_{cav}/c strongly increases from about 0.051 to 0.202. Cavity covers about 1/5 of the foil surface along x direction at C_σ = 1.071.

For the width of the cavity-covered area on foil upper surface w_{cav}, the growth rate $d(w_{cav}/c)/dC_\sigma$ is stable around 0.3. The increasing of w_{cav}/c against C_σ is almost linear. From C_σ = 2.173 to C_σ = 1.071, w_{cav}/c increases from about 0.158 to about 0.636. At C_σ = 1.071, cavity covers more than 3/5 of the half foil surface along the y direction.

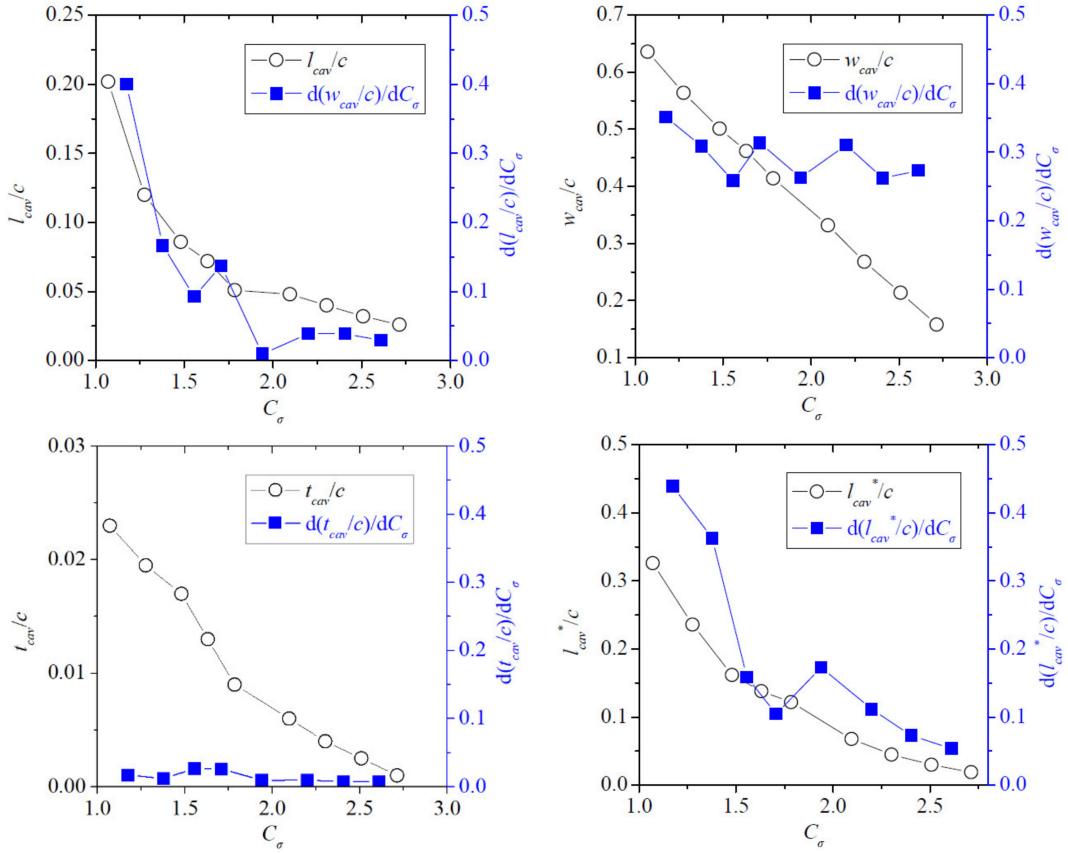

Figure 12. Variation of the length, width and thickness of cavitation bubble on mid-span plane and foil upper surface.

For the maximum thickness of cavity on mid-span t_{cav}, the growth rate is relatively stable. The value of $d(t_{cav}/c)/dC_\sigma$ is lower than 0.03. The increasing of t_{cav}/c against C_σ is almost linear, except in a small range between 1.784 and 1.480. In this range, a special phenomenon occurs in which a tail can be seen on the profile of cavity. This is because of the backward-jet flow (indicated in Figure 13 as an example), and the cavity becomes much thicker. From C_σ = 2.173 to C_σ = 1.071, t_{cav}/c increases from about 0.001 to about 0.023. This thickness (t_{cav}/c = 0.023 at C_σ = 1.071) is about 1/4 of the maximum foil thickness.

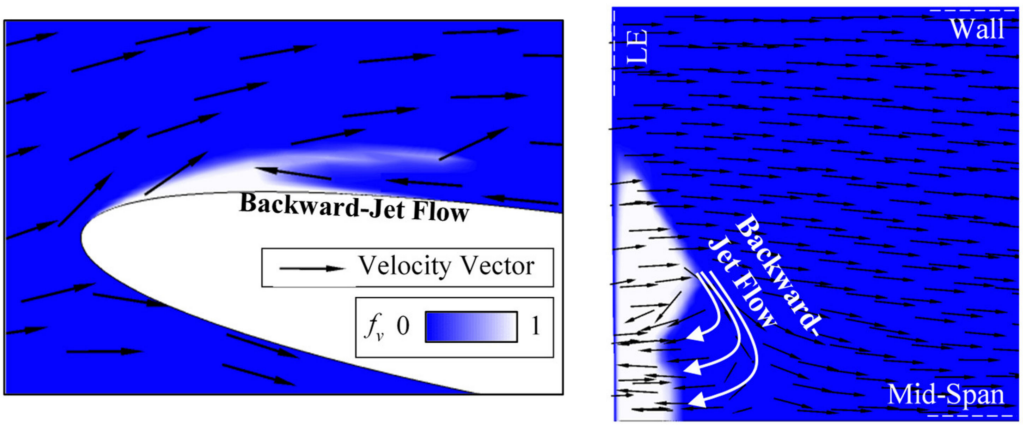

Figure 13. Indication of the backward-jet flow breaking the attached cavity at low C_σ. LE: leading-edge.

For the total length of the attached part of cavity on mid-span l_{cav}^*, the growth rate is similar to l_{cav}. From C_σ = 2.713 to C_σ = 1.480, the value of $d(l_{cav}^*/c)/dC_\sigma$ is lower than 0.2. The value of l_{cav}^* increases from about 0.019 to 0.162. From C_σ = 1.480 to C_σ = 1.071, the

value of $d(l_{cav}^*/c)/dC_\sigma$ is 0.36~0.44. The value of l_{cav}^*/c obviously increases from about 0.162 to 0.326. Comparing with l_{cav}, both the value and the growth rate of l_{cav}^* is higher. This is also because of the tail on cavity. The total length of cavity is bigger than the cavity length covering on foil surface.

Generally, cavitation on a twisted hydrofoil extends along the streamwise direction, spanwise direction and thickness direction with the decreasing of cavitation coefficient C_σ. When C_σ is at a higher level, the small-scale cavity is attached on foil surface. When C_σ becomes lower, cavity on large-incidence-angle spans is broken by the backward-jet from small-incidence-angle spans. A tail is generated on the cavity and the cavity becomes relatively unstable. The growth of cavity becomes quicker, especially in streamwise (length) direction.

7. Conclusions

Based on the above studies and discussions, the conclusions can be drawn as the following two main points:

(1) With the decreasing of cavitation coefficient C_σ, the scale of cavitation continually increases and the increasing is quicker and quicker. The nuclei volume fraction f_{vnuc} has obvious influence on cavitation. The size of cavitation is different at different altitude levels. If the altitude is higher within 0~4000 m, the f_{vnuc} is lower and the size of cavitation is smaller. The difference of the size of cavitation among altitude levels is bigger when C_σ is small. That is, the sensitivity Δf_{cav} is high. On the contrary, the relative sensitivity Δf_{cav}^*, which is the ratio between Δf_{cav} and the absolute cavitation fraction f_{cav}, is high when C_σ is large. When C_σ is 1.071, the Δf_{cav}^* between 0 m and 4000 m altitudes is about 4.6%. When C_σ increases to 2.713, the Δf_{cav}^* can be up to about 22.8%. It means that the cavitation volume fraction sensitivity should be considered in judging the inception cavitation of water pumps and hydro-turbines in the plateau environment.

(2) For this twisted hydrofoil, the installation angle and flow incidence angle are different at different spans. The incoming flow will cause local high pressure on the lower surface of hydrofoil. There will be a local low pressure site on the foil upper surface due to flow separation. This low pressure will cause cavitation. From sidewall to mid-span, the installation angle increases and the minimum pressure decreases. With the decreasing of C_σ, the size of cavitation extends along the spanwise direction, streamwise direction and thickness direction. The growth rate is high in the spanwise (cavity width) and streamwise (cavity length) directions and low in thickness direction. When the size of cavitation is large enough, it will be broken by backflow-jet flow. A tail generates and the cavity becomes relatively unstable.

In general, this study focused on the sensitivity and influence of nuclei fraction on cavitation. The cavitating flow on a twisted hydrofoil was studied in detail. It is helpful for the anti-cavitation design of water pump units and hydro-turbine units installed on plateau.

Author Contributions: Conceptualization, H.L. and R.T.; methodology, H.L. and R.T.; validation, H.L. and R.T.; investigation, H.L. and R.T.; resources, H.L. and R.T.; writing—original draft preparation, H.L. and R.T.; writing—review and editing, H.L. and R.T.; supervision, H.L. and R.T.; project administration, H.L.; funding acquisition, H.L. All authors have read and agreed to the published version of the manuscript.

Funding: This research was funded by the National Natural Science Foundation of China, grant number 51769035.

Institutional Review Board Statement: Not applicable.

Informed Consent Statement: Not applicable.

Data Availability Statement: The data used in this study are available upon request, from the corresponding author.

Conflicts of Interest: The authors declare no conflict of interest.

References

1. Dupont, P. Numerical prediction of cavitation-improving pump design. *World Pumps* **2001**, *83*, 26–28.
2. Arndt, R.E.A. Cavitation in fluid machinery and hydraulic structures. *Annu. Rev. Fluid Mech.* **2003**, *13*, 273–326. [CrossRef]
3. Roussopoulos, K.; Monkewitz, P.A. Measurements of tip vortex characteristics and the effect of an anti-cavitation lip on a model Kaplan turbine blade. *Flow Turbul. Combust.* **2012**, *64*, 119–144. [CrossRef]
4. Čdina, M. Detection of cavitation phenomenon in a centrifugal pump using audible sound. *Mech. Syst. Signal Process.* **2003**, *17*, 1335–1347. [CrossRef]
5. Ni, Y.; Yuan, S.; Pan, Z.; Yuan, J. Detection of cavitation in centrifugal pump by vibration methods. *Chin. J. Mech. Eng.* **2008**, *5*, 50–53. [CrossRef]
6. Wu, S.; Zuo, Z.; Stone, H.A.; Liu, S. Motion of a Free-Settling Spherical Particle Driven by a Laser-Induced Bubble. *Phys. Rev. Lett.* **2017**, *119*, 084501. [CrossRef] [PubMed]
7. Arabnejad, M.H.; Amini, A.; Farhat, M.; Bensow, R.E. Hydrodynamic mechanisms of aggressive collapse events in leading edge cavitation. *J. Hydrodyn.* **2020**, *32*, 6–19. [CrossRef]
8. Tao, R.; Xiao, R.; Farhat, M. Effect of leading edge roughness on cavitation inception and development on thin hydrofoil. *J. Drain. Irrig. Mach. Eng.* **2017**, *35*, 921–926.
9. Dreyer, M.; Decaix, J.; Münch-Alligné, C.; Farhat, M. Mind the gap: A new insight into the tip leakage vortex using stereo-PIV. *Exp. Fluids* **2014**, *55*, 1–13. [CrossRef]
10. Guo, Q.; Zhou, L.; Wang, Z.; Liu, M.; Cheng, H. Numerical simulation for the tip leakage vortex cavitation. *Ocean Eng.* **2018**, *151*, 71–81. [CrossRef]
11. Escaler, X.; Farhat, M.; Avellan, F.; Egusquiza, E. Cavitation erosion tests on a 2D hydrofoil using surface-mounted obstacles. *Wear* **2003**, *254*, 441–449. [CrossRef]
12. Melissaris, T.; Bulten, N.; Terwisga, T.J.C. On the applicability of cavitation erosion risk models with a URANS solver. *J. Fluids Eng.* **2019**, *141*, 101104. [CrossRef]
13. Arakeri, V.H.; Acosta, A.J. Viscous effects in the inception of cavitation on axisymmetric bodies. *J. Fluids Eng.* **1973**, *95*, 519–527. [CrossRef]
14. Morgut, M.; Nobile, E.; Biluš, I. Comparison of mass transfer models for the numerical prediction of sheet cavitation around a hydrofoil. *Int. J. Multiph. Flow* **2011**, *37*, 620–626. [CrossRef]
15. Shi, S.; Wang, G.; Wang, F.; Deming, G. Experimental study on unsteady cavitation flows around three-dimensional hydrofoil. *Chin. J. Appl. Mech.* **2011**, *28*, 105–110.
16. Sear, R.P. Nucleation: Theory and applications to protein solutions and colloidal suspensions. *J. Phys. Condens. Matter* **2007**, *19*, 033101. [CrossRef]
17. Liu, Y.; He, L.; Nie, Q.; Yin, C. Impact of hydropower development on the landscape pattern of Yarlung Zangbo river basin. *Water Power* **2020**, *46*, 1–5.
18. Jaber, J.O. Prospects and challenges of small hydropower development in Jordan. *Jordan J. Mech. Ind. Eng.* **2012**, *6*, 110–118.
19. Feng, C. Monitor of Qinghai-Tibet plateau hydro-thermal circulation with heat pulse. *Acta Geol. Sin.* **2013**, *87*, 631–632.
20. Ahn, S.-H.; Xiao, Y.; Wang, Z.; Zhou, X.; Luo, Y. Numerical prediction on the effect of free surface vortex on intake flow characteristics for tidal power station. *Renew. Energy* **2017**, *101*, 617–628. [CrossRef]
21. Yamamoto, K.; Müller, A.; Favrel, A.; Landry, C.; Avellan, F. Numerical and experimental evidence of the inter-blade cavitation vortex development at deep part load operation of a Francis turbine. *IOP Conf. Ser. Earth Environ. Sci.* **2016**, *49*, 082005. [CrossRef]
22. Ding, H.; Visser, F.; Jiang, Y.; Furmanczyk, M. Demonstration and validation of a 3D CFD simulation tool predicting pump performance and cavitation for industrial applications. *J. Fluids Eng.* **2011**, *133*, 011101. [CrossRef]
23. Zhu, D.; Xiao, R.; Liu, W. Influence of leading-edge cavitation on impeller blade axial force in the pump mode of reversible pump-turbine. *Renew. Energy* **2021**, *163*, 939–949. [CrossRef]
24. Lipej, A.; Mitruševski, D. Numerical Prediction of Inlet Recirculation in Pumps. *Int. J. Fluid Mach. Syst.* **2016**, *9*, 277–286. [CrossRef]
25. Brennen, C.E. *Fundamentals of Multiphase Flow*; Cambridge University Press: Cambridge, UK, 2005.
26. Kubota, A.; Kato, H. Unsteady structure measurement of cloud cavitation on a foil section using conditional sampling techniques. *J. Fluids Eng.* **1989**, *111*, 204–210. [CrossRef]
27. Singhal, A.K.; Athavale, M.M.; Li, H.; Jiang, Y. Mathematical basis and validation of the full cavitation model. *J. Fluids Eng.* **2002**, *124*, 617–624. [CrossRef]
28. Sauer, J.; Schnerr, G.H. Unsteady cavitating flow-A new cavitation model based on a modified front capturing method and bubble dynamics. In Proceedings of the 2000 ASME Fluid Engineering Summer Conference, Boston, MA, USA, 11–15 June 2000.
29. Zwart, P.J.; Gerber, A.G.; Belamri, T. A two-phase flow model for predicting cavitation dynamics. In Proceedings of the Fifth International Conference on Multiphase Flow, Yokohama, Japan, 30 May–3 June 2004.
30. Kunz, R.F.; Boger, D.A.; Stinebring, D.R.; Chyczewski, T.S.; Lindau, J.W.; Gibeling, H.J.; Venkateswaran, S.; Govindan, T.R. A preconditioned Navier–Stokes method for two-phase flows with application to cavitation prediction. *Comput. Fluids* **2000**, *29*, 849–875. [CrossRef]
31. Wang, F. *Analysis Method of Flow in Pumps and Pumping Stations*; China Water & Power Press: Beijing, China, 2020.

32. Bensow, R.E. Simulation of the unsteady cavitation on the Delft Twist11 foil using RANS, DES and LES. In Proceedings of the Second International Symposium on Marine Propulsors, Hamburg, Germany, 15–17 June 2011.
33. Liu, W.; Wei, W.L.; Tian, G.X.; Liu, J.; Liu, Q.H. Research on basic physiological principles of respirator used for plateau areas. *Chin. Med. Equip. J.* **2010**, *31*, 22–36.
34. Menter, F.; Kuntz, M.; Langtry, R. Ten years of industrial experience with the SST turbulence model. *Turbul. Heat Mass Transf.* **2003**, *4*, 625–632.
35. Spalart, P.R. Detached-Eddy Simulation. *Annu. Rev. Fluid Mech.* **2009**, *41*, 181–202. [CrossRef]
36. Vaz, G.; Lloyds, T.; Gnanasundaram, A. Improved Modelling of Sheet Cavitation Dynamics on Delft Twist11 Hydrofoil. In Proceedings of the Seventh International Conference on Computational Methods in Marine Engineering, Nantes, France, 15–17 May 2017.
37. Olshanskii, M.A.; Rebholz, L.G. Velocity–vorticity–helicity formulation and a solver for the Navier–Stokes equations. *J. Comput. Phys.* **2010**, *229*, 4291–4303. [CrossRef]